ADVANCED FUNCTIONAL MATERIALS
www.afm-journal.de

Anisotropic and Heterogeneous Thermal Conductivity in Programmed Liquid Metal Composites Through Direct Ink Writing

Ohnyoung Hur, Eric J. Markvicka, and Michael D. Bartlett**

Thermal management in electric vehicles, electronics, and robotics requires the systematic ability to dissipate and direct the flow of heat. Thermally conductive soft composites are promising for thermal management due to their high thermal conductivity and mechanical flexibility. However, composites typically have the same microstructure throughout a film, which limits directional and spatial control of thermal management in emerging systems that have distributed heat loads. Herein, directional and spatially tunable thermal properties are programmed into liquid metal (LM) soft composites through a direct ink writing (DIW) process. Through the local control of LM droplet aspect ratio and orientation this programmable LM microstructure has a thermal conductivity in the direction of LM elongation of 9.9 W m^{-1}·K^{-1}, which is ~40 times higher than the unfilled elastomer (0.24 W m^{-1}·K^{-1}). The DIW process enables LM droplets to be oriented in specific directions with tunable aspect ratios at different locations throughout a continuous film. This introduces anisotropic and heterogeneous thermal conductivity in compliant films to control the direction and magnitude of heat transfer. This methodology and resulting materials can provide designed thermal management solutions for rigid and soft devices.

1. Introduction

Thermal management in electric vehicles, robotics, and soft electronics is critical, especially with the increasing incorporation of artificial intelligence into these systems.[1–3] To address this challenge, the need for efficient spatial and directional thermal management has become increasingly important.[4,5] Thermal interface materials, which are typically composed of a compliant polymer matrix with thermally conductive rigid inclusions, play a critical role in heat transfer.[6,7] However, the random dispersion of inclusions often results in isotropic behavior.[8,9] One approach to achieve directional thermal control in these soft composites is through controlled microstructures with unidirectionally aligned inclusions.[10,11] This has been achieved through mechanical,[12,13] magnetic,[14,15] and chemical[16] alignment of solid particles. While these approaches improve anisotropic thermal conductivity, incorporating solid particles into a polymer matrix often reduces flexibility, which is important for thermal management.[17] Additionally, this method only provides unidirectional heat control, limiting its ability to manage heat spatially.

Gallium-based liquid metal (LM) has recently been adopted as a thermally conductive inclusion due to its high thermal conductivity and mechanical flexibility.[18–23] In addition to these properties, LM shows multifunctional properties such as

O. Hur, M. D. Bartlett
Mechanical Engineering, Soft Materials and Structures Lab
Virginia Tech
Blacksburg, VA 24061, USA
E-mail: mbartlett@vt.edu
E. J. Markvicka
Mechanical & Materials Engineering, Smart Materials & Robotics Lab
University of Nebraska–Lincoln
Lincoln, NE 68588, USA
E-mail: eric.markvicka@unl.edu

The ORCID identification number(s) for the author(s) of this article can be found under https://doi.org/10.1002/adfm.202417375

DOI: 10.1002/adfm.202417375

E. J. Markvicka
Electrical & Computer Engineering
University of Nebraska–Lincoln
Lincoln, NE 68588, USA
E. J. Markvicka
School of Computing
University of Nebraska–Lincoln
Lincoln, NE 68588, USA
M. D. Bartlett
Macromolecules Innovation Institute
Virginia Tech
Blacksburg, VA 24061, USA

reconfigurability,[24] low viscosity,[25] and low toxicity.[26] These unique attributes have led to the integration of LM soft composites (LMSCs) in various fields, including soft electronics,[27–33] soft robotics,[34–36] stretchable sensors,[37–42] and thermal management applications.[43–45] To fabricate LMSCs, high-shear mixing is a common method for dispersing LMs within elastomers, which results in randomly distributed spherical LM particles and therefore requires additional process steps to program microstructure.[43,46,47] LM droplets can be processed into elongated microstructrues for enhanced thermal conductivity through techniques such as mechanical deformation,[20,48] magnetic alignment,[49–51] or annealing processes.[43,52] However, these approaches require external forces or pre-/post-treatment during or after curing the LM composite to achieve stable microstructures, resulting in uniform (i.e., homogeneous) structures throughout the film, which limits multidirectional heat dissipation control. Alternatively, material extrusion additive manufacturing techniques can program material properties on demand during the printing process.[53–58] For example, direct ink writing (DIW) has been used to create LM microstructures with spherical to elongated inclusions throughout a film without pre-/post-processing or external forces.[42,59–61] By tuning material and printing parameters, this fabrication methodology offers the opportunity for advanced thermal management where properties like thermal conductivity can be programmed during the printing process.

Here, LMSC films with local control of LM microstructure including droplet aspect ratio, orientation, and direction are created through a DIW process for spatially tunable and directional thermal conductivity. This approach creates LM microstructures including spherical and elongated LM droplets throughout a film (**Figure 1a**). By utilizing elongated LM droplets, LMSCs with a high anisotropic thermal conductivity of 9.9 W $m^{-1}{\cdot}K^{-1}$ are achieved, approximately 40× higher than the unfilled elastomer (Figure 1b), while maintaining mechanical flexibility (Figure 1c). By tuning the DIW print path, anisotropic and heterogeneous LM microstructures are programmed at different locations within a film to tune thermal conductivity as a function of position (Figure 1d,e), which enables control of the direction and magnitude of heat transfer across a plane. This control over heat transfer can be observed through infrared (IR) imaging of a high power LED on a film, where the heat dissipation is directional, preferentially transferring the heat generated to a prescribed location (left side) of the film (Figure 1f; Video S1, Supporting Information). This method, which enables tunable and selective heat dissipation by controlling LM microstructures, offers a versatile thermal management solution for applications in thermal diodes, soft electronics, and soft robotics.

2. Results and Discussion

2.1. Isotropic Thermal Conductivity

The thermal conductivity of LM composites is highly dependent on the volume fraction of LM (ϕ, where ϕ = volume of LM/volume of LM and elastomer), the microstructure of the LM (spherical or elongated), and the orientation of the LM (random or aligned). Here, LMSC with different ϕ (0 to 80% with an increase of 10%) were fabricated by casting. The effect of ϕ on the isotropic thermal conductivity ($k_{isotropy}$) of LMSC with a randomly distributed spherical LM microstructure was measured with a modified transient plane source (MTPS, **Figure 2a**). The unfilled elastomer (ϕ = 0%, pristine ExSil) shows a thermal conductivity of 0.24 W $m^{-1}{\cdot}K^{-1}$, whereas the LMSC with ϕ = 80% shows 5.23 W $m^{-1}{\cdot}K^{-1}$, a 22× increase over the unfilled elastomer. The measured thermal conductivity as a function of ϕ agrees well with the Bruggeman effective medium theory (EMT) theory (red dashed line in Figure 2a).[62]

To investigate the effect of droplet size on thermal conductivity, high volume fraction LMSC (ϕ = 60, 70, 80%) were selected. Particle size is then modified by utilizing hexane during the high-shear mixing process to reduce the viscosity of the emulsion during the initial LM droplet formation as the emulsion's viscosity affects droplet size.[46,60,63] The hexane is removed before casting the samples by placing the uncured emulsion into a vacuum chamber for 1.5 h before casting. Hereafter, we define W/ Hx as LMSC modified with hexane, and W/O Hx as unmodified LMSC. The change of LM droplet size (D) was observed through optical microscopy (Figure 2b) and was quantitatively measured through particle image analysis. The distribution of D for W/O Hx LMSC and W/ Hx LMSC are then fitted by a Gaussian distribution and the results are presented in Figure 2c and Figure S1 (Supporting Information). Adding hexane shifts the histogram to the right (increasing D) owing to the temporary decrease of viscosity during mixing. The mean D with a standard deviation, obtained from Gaussian fitting, increased from 84.1 to 228 µm for LMSC (ϕ = 60%) and 46 to 109 µm for LMSC (ϕ = 80%), respectively (Figure 2d). This enables the ability to tune droplet size for a given volume loading.

The $k_{isotropy}$ of W/O Hx and W/ Hx LMSC were measured trough MTPS method (Figure 2e). As shown in Figure 2f, LMSC with a larger D (W/ Hx) showed a slightly higher $k_{isotropy}$ (less than 8%). From this result, controlling droplet size for a given ϕ has a minimal impact on thermal conductivity, so other approaches are needed to enhance thermal conductivity.

2.2. High Anisotropic Thermal Conductivity Achieved by Designing LM Microstructure with DIW Printing

LM droplet shape is a key microstructural component for controlling thermal conductivity.[20,43] We utilize DIW to tune the LM droplet aspect ratio (AR, described in **Figure 3a** inset) by shaping LM droplets directly at the tip of the print nozzle during extrusion. Here, the relative velocity (V*) between the extrusion rate (C) and print head speed (V) is defined as $V^* = V/C$ and is tuned to control droplet AR. We used V^* = 2 to print spherical LM microstructures and V^* = 12 to print elongated LM microstructures. This creates homogeneous samples where the LM microstructure is elongated in one direction, where we define the thermal conductivity in the direction of printing as k_y and the thermal conductivity perpendicular to this direction in plane as k_x and out plane as k_z. We focus on three high LM-loading LMSC (ϕ = 60%, 70%, and 80%) with different droplet size (W/O Hx or W/ Hx) with two different printing conditions (V^* = 2 and 12).

To evaluate the AR of LMs in LMSC, at least 100 particles were analyzed and plotted with a box chart (Figure S2, Supporting

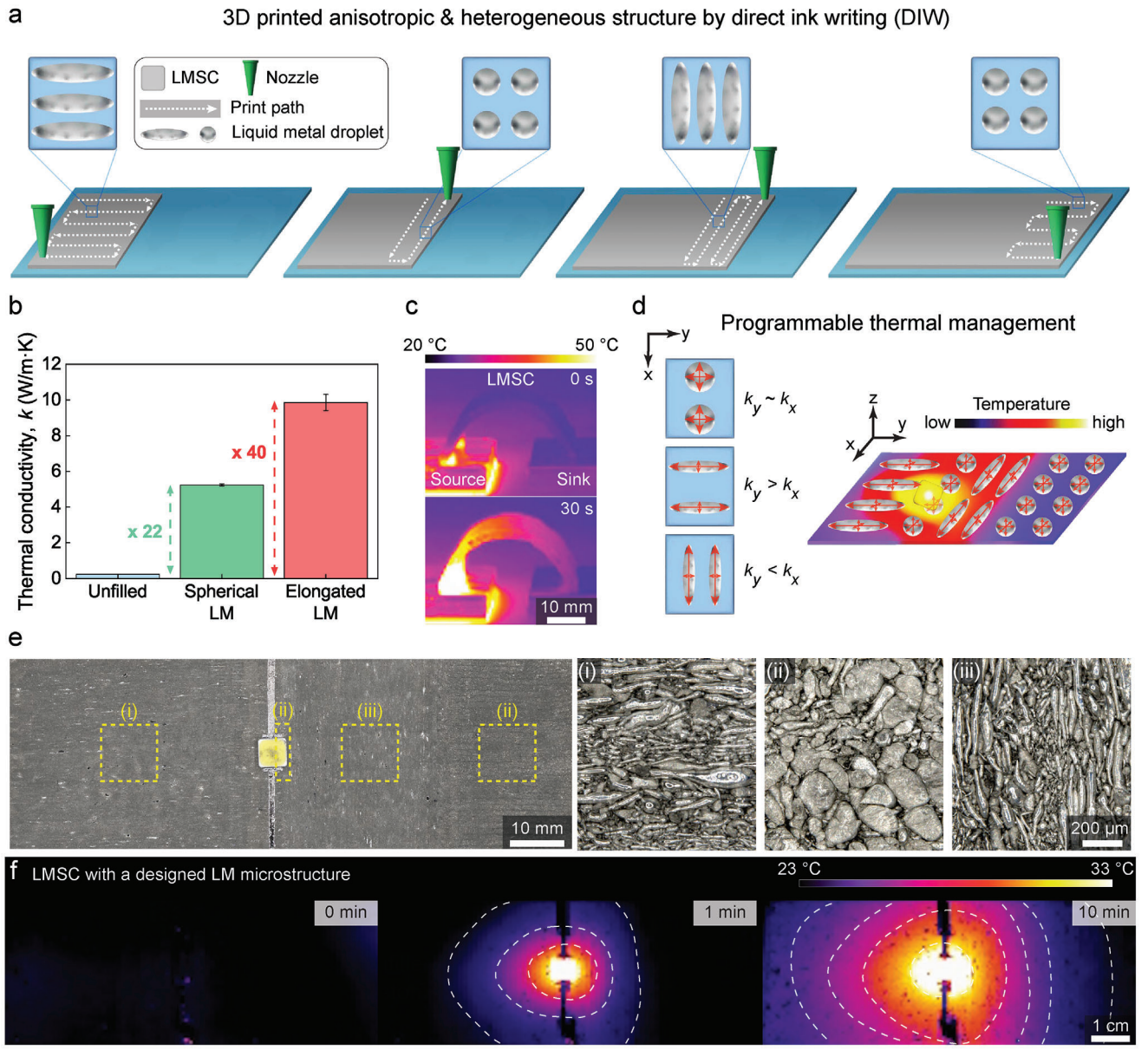

Figure 1. Programmable thermal conductivity by designing LM microstructure through DIW printing. a) Schematic of the DIW printing process to design anisotropic and heterogeneous LM microstructure. The LM droplet schematic shows a top view image. b) Thermal conductivity of three different samples. c) IR images show the flexibility and heat dissipation performance of LMSC with elongated LM. d) Left schematic shows that isotropic/anisotropic thermal conductivity of the LM microstructure. Right schematic shows the anticipated thermal dissipation in the directed path with designed LM microstructures (the yellow square is an LED). e) Optical micrograph of a DIW printed LMSC that includes three different regions. (i) Horizontally elongated LM microstructure. (ii) Spherical LM microstructure. (iii) Vertically elongated LM microstructure. f) IR images with a time sequence of the LMSC with designed microstructures as shown in *e*. The dashed line shows the boundary of different temperature regimes.

Information). The mean value from the box chart of *AR* is presented in Figure 3a–c. *AR* of LMs in LMSC increased with a higher *V** and a larger *D* (W/ Hx). Changes (more elongated LM microstructures) in LM microstructures of LMSC with increased *V** and modification by hexane are presented through optical microscopy images in Figure 3d. Here, we observe that *AR* increases with increasing *V** and *D* (i.e., W/ Hx).

To investigate the anisotropic thermal conductivity (k_y or $k_{x=z}$) of the LMSC, a transient hot wire (THW) method was adopted (Figure 3e). k_{axial} represents the measured thermal conductivity when the platinum (Pt) wire is placed parallel to the alignment of the elongated LMs, while $k_{transverse}$ represents the measured thermal conductivity when Pt wire is placed perpendicular to the orientation of ellipsoidal LMs (Figure 3e). The measured k_{axial} and $k_{transverse}$ for LMSCs are presented in Figure S3 (Supporting Information). These values can be transformed for the calculation of orthotropic bulk properties represented by (k_x, k_y, k_z).[20,64,65] With this transformation, the relationship between anisotropic

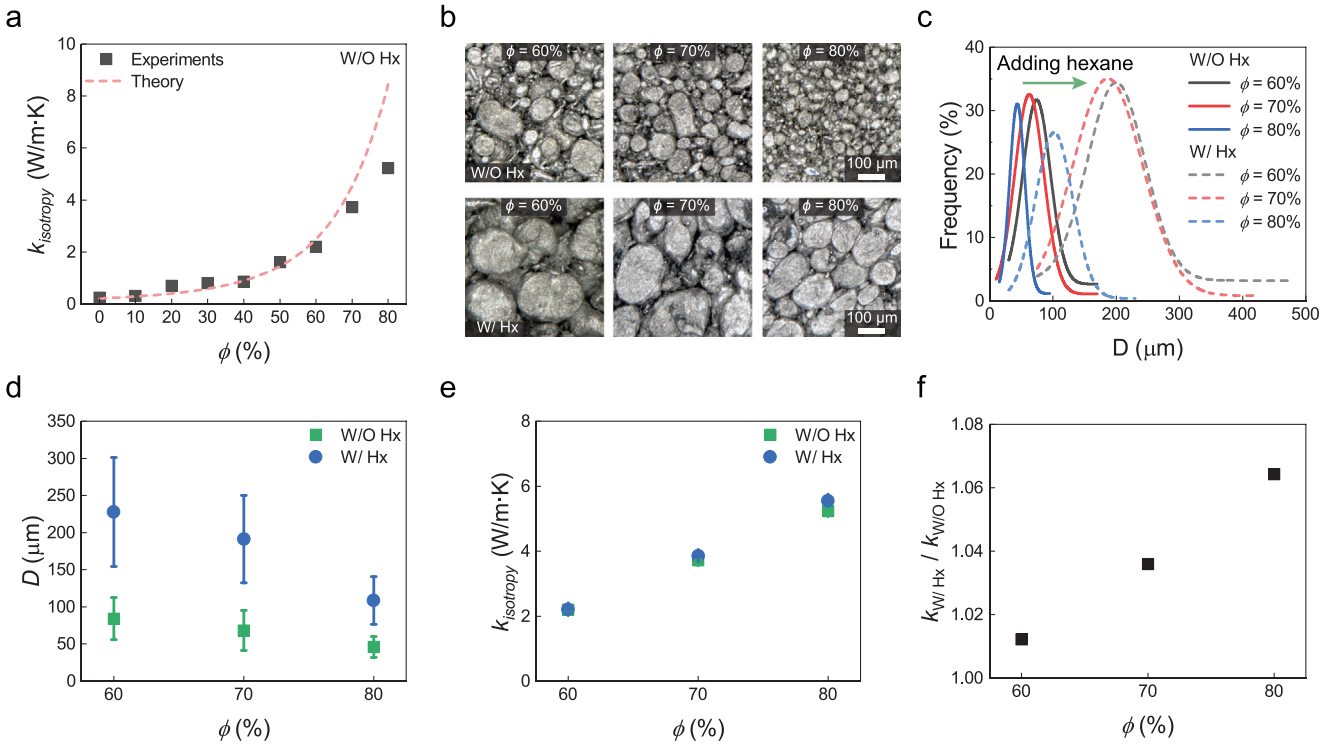

Figure 2. Isotropic thermal conductivity ($k_{isotropy}$) a) $k_{isotropy}$ with different ϕ. ($n = 5$) The dashed line (red) is Bruggeman effective medium theory.[62] ($n = 100$) b) Microscope images of LM droplets unmodified by hexane (W/O Hx, small D) and modified by hexane (W/ Hx, large D) with different ϕ. c) Histogram of LM droplet size (D) of W/O Hx (solid line) and W/ Hx (dashed line) with different ϕ (60%, 70%, and 80%). d) D of different ϕ for W/O Hx (green) and W/ Hx (blue). Error bar is standard deviation ($n \sim 100$). e) $k_{isotropy}$ with different ϕ (60%, 70%, and 80%) for W/O Hx and W/ Hx LMSC. ($n = 5$). f) The $k_{isotropy}$ ratio between W/ Hx and W/O Hx LMSC with different ϕ (60%, 70%, and 80%). Data in *a*, *d*, *e*, and *f* are plotted as the mean ± s.d., if error bars are not visible the data symbol is larger than the error bars.

thermal conductivity and the orientation of elongated LMs can be determined.

Through this analysis method, $k_{x=z}$ is measured and the data are presented with different ϕ in Figure 3f. We find that $k_{x=z}$ increases with ϕ, due to the higher concentration of LM. Furthermore, regardless of the use of hexane or through different printing condition, $k_{x=z}$ was similar for each volume loading as the heat transfer path perpendicular to the elongation droplets was not significantly changed. However, the anistoropic thermal conductivity in the direction of elongation (k_y) shows marked changes with different LM microstructures (Figure 3g). When LMSC has more elongated and aligned LM microstructure (W/ Hx, $V^* = 12$, green), it shows higher k_y than LMSC with spherical microstructure (W/O Hx, $V^* = 2$, black) and LMSC with slightly elongated microstructures (W/O Hx, $V^* = 12$, blue) even though the LMSC includes the same ϕ. Furthermore, W/ Hx, $V^* = 12$, $\phi = 70\%$ shows similar k_y as W/ Hx, $V^* = 12$, $\phi = 80\%$, which we attribute to more elongated LM droplets in the $\phi = 70\%$ sample compared with the $\phi = 80\%$ sample (Figure S4, Supporting Information). As shown in Figure 3h, LMSC ($\phi = 70\%$) showed the highest enhancement in k_y (84%) relative to the same volume loading but with less elongated droplets (W/O Hx, $V^* = 12$). This is because LMSC ($\phi = 70\%$, $V^* = 12$) showed the largest increase (about 88%) in mean AR from 2.32 (W/O Hx, $V^* = 12$) to 4.37 (W/ Hx, $V^* = 12$). LSMC ($\phi = 70\%$, W/ Hx, $V^* = 12$ shows elongated LM microstructure throughout the entire sample (Figure S5, Supporting Information). Therefore, we choose the W/ Hx, $V^* = 12$, $\phi = 70\%$, LMSC composition and processing conditions for heat dissipation demonstration in **Figure 4**. These experiments demonstrate that DIW can effectively program LM microstructure to greatly enhance thermal conductivity. This results in as manufactured LM composites with high thermal conductivities of $k_y = 9.8 \pm 0.88$ W $m^{-1}{\cdot}K^{-1}$ with LMSC ($\phi = 70$ %) manufactured W/Hx and $V^* = 12$. This is approximately 40 times higher than unfilled elastomer, and represents an exceptional combination of high compliance and high thermal conductivity for an as manufactured soft composite.

2.3. Controllable Heat Dissipation Path with Designed LM Microstructure Through DIW

Through the DIW process, we can create highly elongated microstructures throughout soft films by tuning the process conditions. We can orient the LM droplets in different directions on demand by controlling the print path, while also using materials that enable stretchability and flexibility as shown in Figure S6 (Supporting Information). This provides a unique opportunity to create soft thermal films that have prescribed anisotropic and spatially varying properties for heterogeneous structures that control the direction and magnitude of heat conduction.

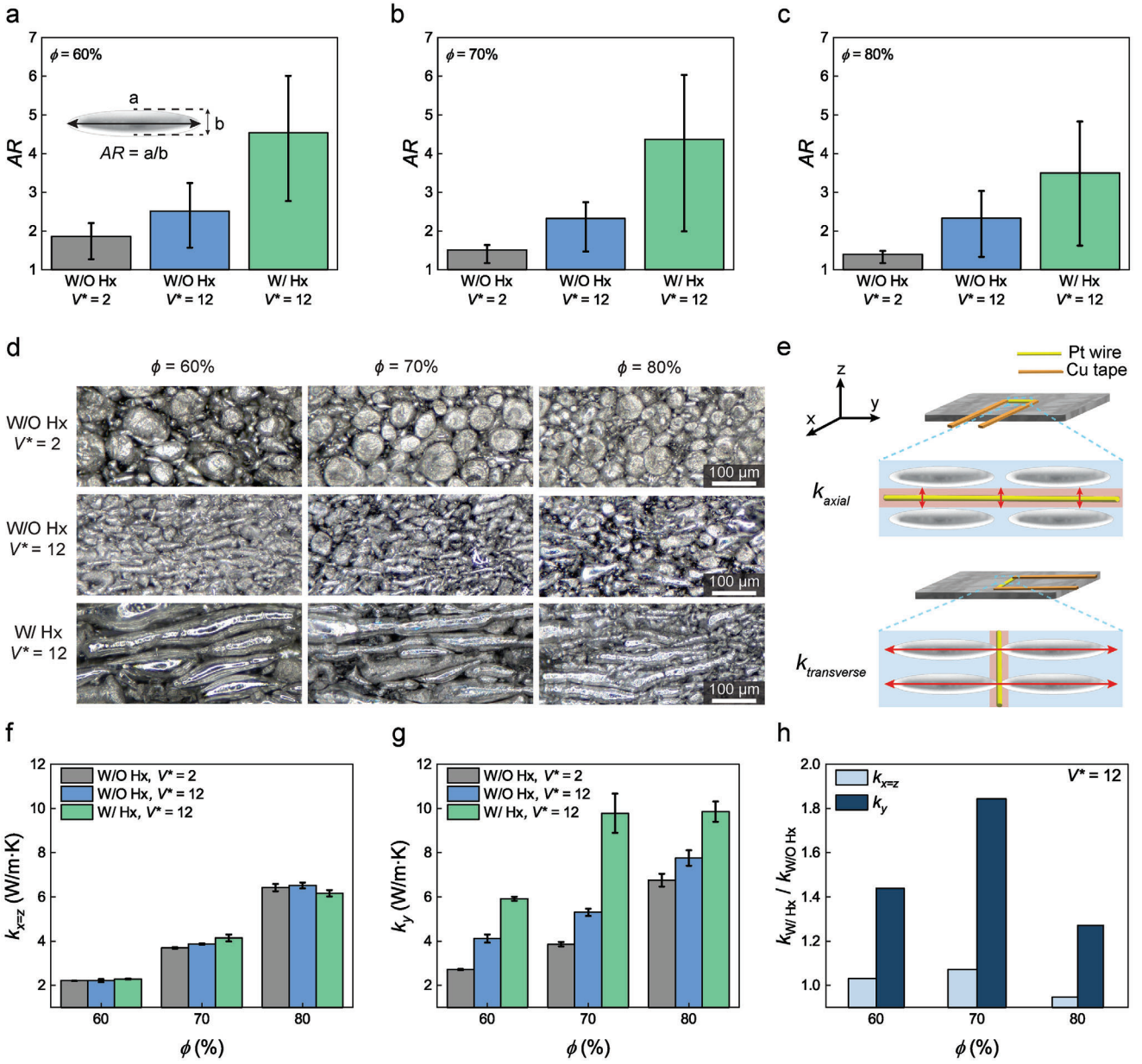

Figure 3. Anisotropic thermal conductivity of DIW printed LMSC. Aspect ratio (*AR*) for different ϕ, *D* (W/O Hx or W/ Hx), and printing conditions ($V^* = 2$ or 12) a) $\phi = 60\%$, b) $\phi = 70\%$, and c) $\phi = 80\%$. Upper error bar is *Q*3 and lower error bar is *Q*1 from the box plot (See the details in Figure S2, Supporting Information). d) Microscope images of LMSC presented in *a-c*. e) A schematic showing the measurement of anisotropic thermal conductivity (k_{axial} and $k_{transverse}$) to get k_x, k_y, and k_z. Anisotropic thermal conductivity for f) $k_{x=z}$ and g) for k_y with different ϕ (60% to 80%). h) The ratio of anisotropic thermal conductivity between small *D* (W/O Hx) and large *D* (W/ Hx) for different ϕ.

To demonstrate this capability, we designed an LMSC (W/ Hx, ϕ = 70%) with three distinct LM-microstructures regions. We define these as region (i), horizontally elongated LM droplets, region (ii), vertically elongated LM droplets, and region (iii), spherical LM droplets (Figure 4a). Microscope images show each region with programmed LM microstructures in Figure 4b. The LMSC with a designed structure still demonstrates mechanical flexibility, as shown in Figure 4c. To evaluate the microstucture control of heat dissipation, two different samples (unfilled elastomer and LMSC with the designed structure) were tested with a high power LED at room temperature (Figure 4d and Figure S7; Video S1, Supporting Information). The LED was placed in the same location for all samples on the right edge of region (i), as shown in Figure 4a and d. The same power (3.7V and 0.35A) was applied to the LED in all cases to turn on the LED at the beginning. As shown in Figure 4d and e, the heat dissipation from the LED is different between each sample (unfilled elastomer and LMSC (designed)). For example, the unfilled elastomer showed heat accumulation around the LED as it has a low thermal conductivity (0.24 W $m^{-1}{\cdot}K^{-1}$) which resulted in poor heat

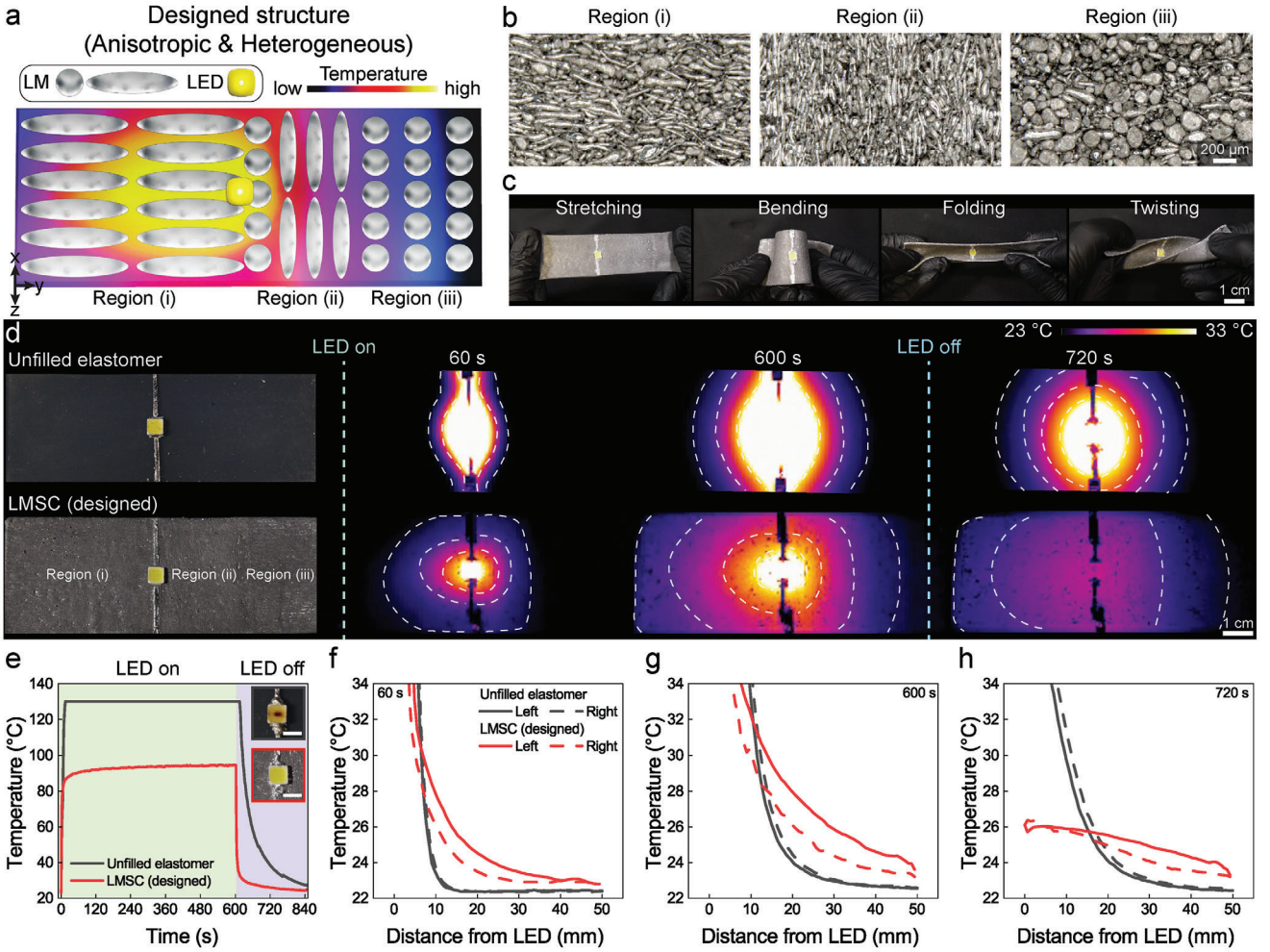

Figure 4. Controllable heat dissipation with designed LM microstructure. a) Schematic for a designed LM microstructure with three different microstructures, region (i), region (ii), and region (iii). The color map shows the anticipated heat dissipation with the designed microstructures. b) Microscope images for three different regions in the designed LM structure. c) Images show mechanical flexibility of LMSC (designed). d) Optical images (left) and IR images (right) of heat dissipation test of two different samples, unfilled elastomer and LMSC with designed LM microstructures. e) The temperature (°C) changes with time (s) of each samples at LED. Inset images showed LEDs after 600 s operation (top: unfilled elastomer, bottom: LMSC (designed)). Scale bars are 3 mm. Temperature (°C) changes with a distance (mm) from LED: after f) 60 s and g) 600 s with the LED on. h) After 120 s with the LED off. The solid lines represent the temperature measurement at the left region of the LED, while the dashed lines represent the temperature measurement at the right region of the LED. *g* and *h* follow legend in *f*.

conduction and dissipation that resulted a damage in the LED (a top inset in Figure 4e). However, the LMSC with designed inclusions showed better heat conduction and dissipation properties without any damage on LED (a bottom inset in Figure 4e) as they have high thermal conductivity. In addition, the LMSC with a designed structure exhibited directed heat conduction along a desired pathway. Here the LM inclusions in region (i) are oriented in y axis, which results in enhanced y-directional thermal conductivity relative to region (ii) where the LM inclusions are aligned to x axis. This creates an ellipsoidal thermal distribution in region (i), where heat is preferentially transferred along the y-axis due to the programmed elongated microstructures. However, a radial-like thermal distribution occurs within an unfilled elastomer and a LMSC with random (spherical LM microstructure) in regions (ii) and (iii) (see 60 s (s), 600 s IR images in Figure 4d; Figure S8, Supporting Information). When the LED was turned off, the cooling property was also improved in the LMSC sample compared with the unfilled sample (Figure 4e).

To quantitatively evaluate the anisotropic heat dissipation performance, temperature changes at a different location in each sample are plotted in Figure 4f–h. As shown in Figure 4f, the LMSC with a designed structure showed a higher temperature than unfilled elastomer at almost regions (at distance $>\approx 10$ mm) due to its greater thermal conductivity. Furthermore, compared with the unfilled elastomer which has isotropic heat dissipation properties, LMSC with a designed structure showed higher temperatures in the left region than in the right, as it possesses anisotropic heat dissipation properties. This is attributed to the designed heat transfer path toward the left, facilitated by the elongated LM microstructure in that direction. For 600 s after turning on the LED, the LMSC with a designed structure exhibited higher anisotropic heat dissipation performance (a larger temperature

gap between the left and right regions), while the unfilled elastomer showed continuous isotropic heat dissipation properties (Figure 4g). Additionally, the LMSC with a designed structure exhibited better cooling properties at all locations compared with the unfilled elastomer after turning off the LED, due to its high thermal conductivity (Figure 4h). These results demonstrate that by designing the LM microstructure, effective anistoropic heat dissipation can be achieved.

The ability to print a range of LM droplet microstructures–ranging from homogeneous to heterogeneous–using a single ink and manufacturing system enables the creation of soft elastomer composites with tailored, anisotropic and heterogeneous thermal conductivity and heat transfer characteristics. This enables the control of heat flow within soft composite materials, towards preventing the thermal degradation of sensitive parts or electronic components to enhance their lifespan.

3. Conclusion

This work demonstrates LMSC with anisotropic and heterogeneous LM microstructures for thermal management systems with spatial and local heat control. These microstructures are achieved through a DIW process where they are directly manufactured and no pre-/post-processing are required to maintain or design LM microstructures. Controlling the LM droplet microstructure is performed directly at the print nozzle tip, which is attributed to the unique ability of the LM droplets to transform during the DIW process. By combining the control of LM inclusion elongation and the ability of high volume loading of inclusions, a highly anisotropic thermal conductivity of 9.9 ± 0.46 W $m^{-1}{\cdot}K^{-1}$ is achieved, which is approximately 40× higher than the unfilled elastomer. By leveraging this material system within the DIW process, we presented the ability to locally design LM microstructural features such as aspect ratio and orientation. This overcomes challenges in previous processing techniques where LM microstructure is either spherical or show a uniform (i.e., homogeneous) microstructure across the sample. This capability opens new avenues to design thermal management by programming different thermal capabilities within a film through a single process and a single ink. We anticipate that this will provide insight into soft materials for directional heat transfer that can be used to control thermal dissipation in emerging device architectures.

4. Experimental Section

Materials and Ink Fabrication: Eutectic gallium indium (EGaIn) was fabricated by mixing In:Ga in a weight ratio of 1:3, homogenized on a hot plate at 200 °C overnight. LM inks were prepared through a two-step process. Initially, the ink was manually mixed using a glass rod. Subsequently, to achieve uniform dispersion of LM droplets in ExSil 100 (Gelest Inc.), a planetary centrifugal mixer (DAC 1200-500 VAC, FlackTek speed mixer) was employed. The mixing process was conducted at 800 rpm for 1 min in a vacuum environment to remove air bubbles. For the fabrication of inks with large *D* LM droplets, hexane was added to the uncured ExSil in a 1:8 weight ratio and premixed before introducing LM. The LM was then dispersed using the FlackTek speed mixer under the same mixing conditions (800 rpm for 1 min). Finally, the inks were placed in a vacuum chamber for 1.5 h to eliminate any remaining hexane before the DIW printing process.

Casting Process: The mixed inks were poured into a clear acrylic plate with dimensions of 25 × 25 × 2 mm and covered by a acrylic plate then gently pressed with clamps to create an even surface. Subsequently, the ink in the mold was cured in a convection oven at 80 °C overnight.

Fabrication of LMSC by DIW Process: The prepared ink was loaded into a syringe (BD 10mL syringe) with a tapered nozzle featuring an inner diameter of 0.84 mm. The syringe filled with LM inks was inserted into a material extrusion system (Hyrel SR 3D printer) equipped with an SDS-10 syringe head. Multilayer samples were then printed on sandpaper (600 Grit), with each sample having dimensions of 25 × 25 × 2 mm. The extrusion rate was set at 4.1 mm s^{-1} for both $V^* = 2$ and 12. The print head velocity was 8.1 and 49.2 mm s^{-1} for $V^* = 2$ and 12, respectively. To achieve the desired extrusion rate and print head velocity, these values were calculated based on the printed trace length and the syringe and nozzle inner diameters. The calculated values were then included in the G-code. The print height was 210 µm and 50 µm for $V^* = 2$ and 12, respectively. In the interval between printing each layer, a convection heating process using a 130 °C heat gun was applied for 3 min, followed by a cooling period using a cooling fan for 1 min. Upon completing the multilayer printing, the printed samples were fully cured overnight in a convection oven set at 80 °C.

Optical Microscopy: Surface images of the printed samples were captured using an optical microscope (Zeiss Axiozoom v16 stereomicroscope). The morphology analysis of the LM droplets was conducted on the microscope images through Image J software. The outlines of the LM droplets were manually traced and converted into a binary image, distinguishing between elastomer and LM droplet areas. Subsequently, an ellipse fit was applied to each LM droplet section, for the extraction of major (a) and minor (b) axis length (inset images in Figure 3a). The major axis was considered the LM droplet size (*D*) for spherical droplets. The *AR* of the LM droplet was calculated by determining the ratio of the major to the minor axis of the fitted ellipse. To analyze the *AR* distribution of LM droplets in the printed structure, box plots were used (Figure S2, Supporting Information).

Measurement of Thermal Conductivity: A C-Therm Trident model (MTPS method) was utilized to measure the isotropic thermal conductivity of the cast samples at room temperature.[66] The sample size was 25 × 25 × 2 mm. The anisotropic thermal conductivity (k_{axial} and $k_{transverse}$) was determined using the THW method. From these values, k_y and $k_{x=z}$ were calculated as in previous work.[20] The sample size for this measurement was the same as that of the casting sample. This measurement process was repeated five times with 1 min intervals to allow the sample to dissipate any residual heat from the previous test. The presented thermal conductivity is an average value from five different runs, along with a standard deviation.

LED Demonstration to Evaluate Designed Heat Dissipation Behaviors: To investigate the directed heat dissipation based on LM microstructure, three different samples were tested: unfilled, LMSC with random and designed structures. The unfilled sample and LMSC with random structure were produced through a casting process. Unfilled ExSil or LM ink (ϕ = 70%) was poured into a mold (dimensions: 100 × 35 × 2.5 mm) and cured in an oven at 80 °C overnight. To fabricate LMSC with designed structures (Figure 4a), hexane was temporarily added to modify the LM ink ($\phi = 70\%$) viscosity to achieve a large *D*. All hexane was removed using a vacuum chamber for 1.5 h before usage. The Hyrel 3D printer was adopted to print the designed structure, with the same printing conditions as described in the fabrication of LMSC by DIW process section. For the region (i) and region (ii), V^* was set to 12, and a print height of 50 µm was utilized. For the region (iii) section, V^* was set to 2, and a print height of 210 µm was used. The region (i) section had dimensions of 50 × 35 mm, while the region (ii) and region (iii) sections had dimensions of 25 × 35 mm. The structure thickness was approximately 2.5 mm (50 layers for region (i) and region (ii), 12 layers for region (iii)). To assess the heat dissipation behavior, an LED (CreeLED, Inc.) was placed on the right edge of region (i) section for all samples. LM-Cu paste was utilized as electrodes to connect the LED to the power supply (RD6018, RIDEN). The LED was powered with a voltage of 3.7V and a current of 0.35A. An IR camera (E54sc, FLIR) recorded the heat dissipation properties with emissivity of 0.9 and reflection temperature = 20 °C. The LED was activated for 10 min, then turned off, and left

for 5 minutes to evaluate the cooling properties. The limitation of the IR camera (the measurable maximum temperature is 130 °C) resulted in a temperature plateau in unfilled sample around 130 °C in Figure 4e.

Supporting Information

Supporting Information is available from the Wiley Online Library or from the author.

Acknowledgements

O.H. and M.B. acknowledge support through NSF (No. CMMI-2054409). E.M. acknowledges support through the NSF (No. CMMI-2054411).

Conflict of Interest

The authors declare no conflict of interest.

Data Availability Statement

The data that support the findings of this study are available from the corresponding author upon reasonable request.

Keywords

anisotropy, direct ink writing, heterogeneous, liquid metal, thermal conductivity

Received: September 16, 2024
Revised: November 8, 2024
Published online:

[1] E. Sevinchan, I. Dincer, H. Lang, *Appl. Therm. Eng.* **2018**, *140*, 799.
[2] G. Moreno, S. Narumanchi, X. Feng, P. Anschel, S. Myers, P. Keller, *J. Electron. Packag.* **2022**, *144*, 011004.
[3] H. Liu, A. Aljbri, J. Song, J. Jiang, C. Hua, *Tsinghua Sci. Technol.* **2021**, *27*, 303.
[4] A. R. Dhumal, A. P. Kulkarni, N. H. Ambhore, *J. Eng. Appl. Sci.* **2023**, *70*, 140.
[5] Z. Zhang, X. Wang, Y. Yan, *e-Prime-Adv. Electrical Eng. Electron. Energy* **2021**, *1*, 100009.
[6] J. Khan, S. A. Momin, M. Mariatti, *Carbon* **2020**, *168*, 65.
[7] Y. Zhang, J. Ma, N. Wei, J. Yang, Q.-X. Pei, *Phys. Chem. Chem. Phys.* **2021**, *23*, 753.
[8] M. Qin, Y. Xu, R. Cao, W. Feng, L. Chen, *Adv. Funct. Mater.* **2018**, *28*, 1805053.
[9] Y. Xue, X. Zhou, T. Zhan, B. Jiang, Q. Guo, X. Fu, K. Shimamura, Y. Xu, T. Mori, P. Dai, Y. Bando, C. Tang, D. Golberg, *Adv. Funct. Mater.* **2018**, *28*, 1801205.
[10] W. Wu, T. Ren, X. Liu, R. Davis, K. Huai, X. Cui, H. Wei, J. Hu, Y. Xia, S. Huang, Z. Qiang, K. (Kelvin) Fu, J. Zhang, Y. Chen, *Compos. Commun.* **2022**, *35*, 101309.
[11] Y. Xue, H. Wang, X. Li, Y. Chen, *Composites, Part A* **2021**, *144*, 106336.
[12] C. Yu, W. Gong, W. Tian, Q. Zhang, Y. Xu, Z. Lin, M. Hu, X. Fan, Y. Yao, *Compos. Sci. Technol.* **2018**, *160*, 199.
[13] Y. Xue, X. Li, H. Wang, F. Zhao, D. Zhang, Y. Chen, *Mater. Des.* **2019**, *165*, 107580.
[14] C. Yuan, B. Duan, L. Li, B. Xie, M. Huang, X. Luo, *ACS Appl. Mater. Interfaces* **2015**, *7*, 13000.
[15] K. Kim, J. Kim, *Int. J. Therm. Sci.* **2016**, *100*, 29.
[16] M. C. Vu, W.-K. Choi, S. G. Lee, P. J. Park, D. H. Kim, M. A. Islam, S.-R. Kim, *ACS Appl. Mater. Interfaces* **2020**, *12*, 23388.
[17] R. Tutika, S. H. Zhou, R. E. Napolitano, M. D. Bartlett, *Adv. Funct. Mater.* **2018**, *28*, 1804336.
[18] K.-Q. Ma, J. Liu, *J. Phys. D: Appl. Phys.* **2007**, *40*, 4722.
[19] S. Mei, Y. Gao, Z. Deng, J. Liu, *J. Electron. Packag.* **2014**, *136*, 011009.
[20] M. D. Bartlett, N. Kazem, M. J. Powell-Palm, X. Huang, W. Sun, J. A. Malen, C. Majidi, *Proc. Natl. Acad. Sci. USA* **2017**, *114*, 2143.
[21] X. Wang, C. Lu, W. Rao, *Appl. Therm. Eng.* **2021**, *192*, 116937.
[22] E. J. Krings, H. Zhang, S. Sarin, J. E. Shield, S. Ryu, E. J. Markvicka, *Small* **2021**, *17*, 2104762.
[23] P. Won, C. S. Valentine, M. Zadan, C. Pan, M. Vinciguerra, D. K. Patel, S. H. Ko, L. M. Walker, C. Majidi, *ACS Appl. Mater. Interfaces* **2022**, *14*, 55028.
[24] M. D. Dickey, *ACS Appl. Mater. Interfaces* **2014**, *6*, 18369.
[25] M. Khondoker, D. Sameoto, *Smart Mater. Struct.* **2016**, *25*, 093001.
[26] S. Chen, R. Zhao, X. Sun, H. Wang, L. Li, J. Liu, *Adv. Healthcare Mater.* **2023**, *12*, 2201924.
[27] M. D. Dickey, *Adv. Mater.* **2017**, *29*, 1606425.
[28] R. Tutika, A. T. Haque, M. D. Bartlett, *Commun. Mater.* **2021**, *2*, 64.
[29] E. J. Krings, B. D. Hage, S. L. Truong, K. A. Reeser, E. L. Fox, M. G. Snyder, Q. Walker, G. R. Bashford, E. J. Markvicka, *Adv. Funct. Mater.* **2023**, 2308954.
[30] M. H. Malakooti, N. Kazem, J. Yan, C. Pan, E. J. Markvicka, K. Matyjaszewski, C. Majidi, *Adv. Funct. Mater.* **2019**, *29*, 1906098.
[31] R.-M. Chin, Y. Han, M. H. Malakooti, *Adv. Mater. Technol.* **2024**, *9*, 2301324.
[32] M. J. Ford, D. K. Patel, C. Pan, S. Bergbreiter, C. Majidi, *Adv. Mater.* **2020**, *32*, 2002929.
[33] D. H. Ho, C. Hu, L. Li, M. D. Bartlett, *Nat. Electron.* **2024**, 1.
[34] X. Wang, R. Guo, J. Liu, *Adv. Mater. Technol.* **2019**, *4*, 1800549.
[35] L. Zheng, S. Handschuh-Wang, Z. Ye, B. Wang, *Appl. Mater. Today* **2022**, *27*, 101423.
[36] E. J. Markvicka, M. D. Bartlett, X. Huang, C. Majidi, *Nat. Mater.* **2018**, *17*, 618.
[37] Y. Y. Choi, D. H. Ho, J. H. Cho, *ACS Appl. Mater. Interfaces* **2020**, *12*, 9824.
[38] O. Gul, K. Kim, J. Gu, J. Choi, D. Del Orbe Henriquez, J. Ahn, I. Park, *ACS Appl. Electron. Mater.* **2021**, *3*, 4027.
[39] K. Kim, J. Ahn, Y. Jeong, J. Choi, O. Gul, I. Park, *Micro Nano Systems Letters* **2021**, *9*, 1.
[40] K. Kim, J. Choi, Y. Jeong, I. Cho, M. Kim, S. Kim, Y. Oh, I. Park, *Adv. Healthcare Mater.* **2019**, *8*, 1900978.
[41] E. M. Abbara, M. Alhendi, R. Al-haidari, N. Gee, M. D. Poliks, E. Boggs, T. Yewteck, D. Trivedi, Z. j. Farrell, C. E. Tabor, in *2023 IEEE 73rd Electronic Components and Technology Conference (ECTC)*, IEEE, **2023**, pp. 426–431.
[42] S. Pak, M. D. Bartlett, E. J. Markvicka, *Adv. Funct. Mater.* **2024**, 202410908.
[43] A. T. Haque, R. Tutika, R. L. Byrum, M. D. Bartlett, *Adv. Funct. Mater.* **2020**, *30*, 2000832.
[44] J. Mingear, Z. Farrell, D. Hartl, C. Tabor, *Nanoscale* **2021**, *13*, 730.
[45] T. A. Pozarycki, W. Zu, B. T. Wilcox, M. D. Bartlett, *Adv. Funct. Mater.* **2024**, 2313567.
[46] A. Koh, J. Sietins, G. Slipher, R. Mrozek, *J. Mater. Res.* **2018**, *33*, 2443.
[47] R. Tutika, S. Kmiec, A. T. Haque, S. W. Martin, M. D. Bartlett, *ACS Appl. Mater. Interfaces* **2019**, *11*, 17873.
[48] C. Pan, E. J. Markvicka, M. H. Malakooti, J. Yan, L. Hu, K. Matyjaszewski, C. Majidi, *Adv. Mater.* **2019**, *31*, 1900663.
[49] S. Kim, S. Kim, K. Hong, M. D. Dickey, S. Park, *ACS Appl. Mater. Interfaces* **2022**, *14*, 37110.

[50] R. Zhu, Z. Li, G. Deng, Y. Yu, J. Shui, R. Yu, C. Pan, X. Liu, *Nano Energy* **2022**, *92*, 106700.
[51] G. Yun, S.-Y. Tang, Q. Zhao, Y. Zhang, H. Lu, D. Yuan, S. Sun, L. Deng, M. D. Dickey, W. Li, *Matter* **2020**, *3*, 824.
[52] S. Chen, W. Xing, H. Wang, W. Cheng, Z. Lei, F. Zheng, P. Tao, W. Shang, B. Fu, C. Song, M. D. Dickey, T. Deng, *Chem. Eng. J.* **2022**, *439*, 135674.
[53] D. B. Kolesky, R. L. Truby, A. S. Gladman, T. A. Busbee, K. A. Homan, J. A. Lewis, *Adv. Mater.* **2014**, *26*, 3124.
[54] A. Kotikian, R. L. Truby, J. W. Boley, T. J. White, J. A. Lewis, *Adv. Mater.* **2018**, *30*, 1706164.
[55] D. J. Braconnier, R. E. Jensen, A. M. Peterson, *Addit. Manuf.* **2020**, *31*, 100924.
[56] T. Nasrin, M. Pourali, F. Pourkamali-Anaraki, A. M. Peterson, *Sci. Rep.* **2023**, *13*, 11460.
[57] L. T. Smith, R. B. MacCurdy, *Adv. Mater.* **2024**, 2308491.
[58] L. Smith, B. Hayes, K. Ford, E. Smith, D. Flores, R. MacCurdy, *Adv. Mater. Technol.* **2024**, *9*, 2301668.
[59] A. Haake, R. Tutika, G. M. Schloer, M. D. Bartlett, E. J. Markvicka, *Adv. Mater.* **2022**, *34*, 2200182.
[60] O. Hur, R. Tutika, N. Klemba, E. J. Markvicka, M. D. Bartlett, *Addit. Manuf.* **2023**, 103925.
[61] W. Zu, H. E. Carranza, M. D. Bartlett, *ACS Appl. Mater. Interfaces* **2024**.
[62] V. D. Bruggeman, *Ann. Phys.* **1935**, *416*, 636.
[63] I. D. Tevis, L. B. Newcomb, M. Thuo, *Langmuir* **2014**, *30*, 14308.
[64] T. Ohmura, M. Tsuboi, T. Tomimura, *Int. J. Thermophys.* **2002**, *23*, 843.
[65] T. Borca-Tasciuc, A. Kumar, G. Chen, *Rev. Sci. Instrum.* **2001**, *72*, 2139.
[66] A. D7984-16, Standard test method for measurement of thermal effusivity of fabrics using a modified transient plane source (mtps) instrument, **2016**.